Applied Catalysis B: Environmental 304 (2022) 121014

Contents lists available at ScienceDirect

Applied Catalysis B: Environmental

journal homepage: www.elsevier.com/locate/apcatb

Phosphate ions interfacial drift layer to improve the performance of CoFe−Prussian blue hematite photoanode toward water splitting

Abdul Zeeshan Khan [a], Tarek.A. Kandiel [a,b,*], Safwat Abdel-Azeim [c], Tahir Naveed Jahangir [a], Khalid Alhooshani [a]

[a] Department of Chemistry, King Fahd University of Petroleum & Minerals (KFUPM), Dhahran 31261, Saudi Arabia
[b] Interdisciplinary Research Center for Hydrogen and Energy Storage (IRC-HES) at KFUPM, Dhahran 31261, Saudi Arabia
[c] Center for Integrative Petroleum Research (CIPR), College of Petroleum Engineering and Geosciences (CPG) KFUPM, Dhahran 31261, Saudi Arabia

ARTICLE INFO

Keywords:
Hematite Photoanodes
Prussian blue analogue (PBA) OER catalyst
Phosphate ions (Pi) interfacial layer
IMPS

ABSTRACT

Charge recombination at the surface of hematite photoanode is among the main issues that diminish its photoelectrochemical (PEC) water splitting efficiency. Herein, we address this issue by anchoring phosphate ions (Pi) layer between hematite's surface and CoFe−Prussian blue analogue (CoFe−PBA) water oxidation catalyst (WOC). The PEC results revealed that the Pi interfacial layer is crucial for boosting the PEC activity of CoFe−PBA/hematite photoanode. It improves the activity by 2.9-fold at 1.23 V_{RHE}. The analysis of time and frequency-resolved results revealed that the synergy between the Pi layer and CoFe−PBA catalyst prolongs the photogenerated holes lifetime, reduces their charge transfer resistance, and suppresses the surface recombination. The DFT simulations suggested that the Pi interfacial layer drifts the electrostatic potential of the hematite's surface toward more negative potential and thus facilities the diffusion of the photogenerated holes toward the hematite/CoFe−PBA/electrolyte interfaces making them dynamically apposite to oxidize water on CoFe−PBA WOC.

1. Introduction

Photoelectrochemical (PEC) cells are among the best promising approaches to mimic the natural photosynthesis process in harvesting and storing solar energy as chemical fuels [1]. Consequently, the PEC water splitting has attracted more consideration as a potential technology for storing solar energy as H_2 chemical fuel with zero carbon dioxide emission. However, the high rate of charge carriers recombination and slow kinetics of water oxidation at the most of photoelectrode surfaces limit the overall PEC water splitting efficiency [2]. Water oxidation involves multi-hole transfer processes and thus long-life holes are required to produce molecular oxygen [3]. Besides, the need to accelerate the kinetics of water oxidation, the ideal photoanodes should have also low cost, high stability, suitable band structure, and excellent light-harvesting properties. Despite substantial improvement in the field of PEC water splitting, photoanodes that satisfy all those constraints have not been discovered yet. Thus, the amendment of the current known photoelectrodes is required to minimize the recombination of charge carriers, improve the charge transfer efficiency, and catalyze the water oxidation process. The most appropriate n-type semiconductor materials, which are commonly employed as photoanodes in the PEC cells, are metal oxide such as TiO_2 [4], α-Fe_2O_3 [5], WO_3 [6], and $BiVO_4$ [7] due to their high chemical stability. Out of them, α-Fe_2O_3 (hematite) is considered to be very appealing due to many distinct merits such as environmentally benign nature, stability in the water at a wide range of pH (i.e., 4−14), abundantly available in earth crust (6.3 wt%), and its valence band potential matches perfectly the thermodynamic requirements for water oxidation [8]. Moreover, hematite exhibits a bandgap of 1.9 – 2.2 eV and thus absorbs about 40% of the solar spectrum and theoretically can generate 12.6 mA cm^{-2} at standard test conditions (STC, 1.0 sun, and AM 1.5 G) [8,9]. Nevertheless, the PEC activity of hematite is still limited by the rapid charge carriers recombination in the bulk, the short diffusion length of photogenerated holes (i.e., 2 – 4 nm), and the high rate of surface recombination [10,11]. In particular, the fast surface recombination limits the accessibility of holes at the surface and thus suppresses the rate of water oxidation.

To overcome these limitations, various methodologies (e.g. heterojunction fabrication, elemental doping, morphology engineering, and

* Corresponding author at: Department of Chemistry, King Fahd University of Petroleum & Minerals (KFUPM), Dhahran 31261, Saudi Arabia.
E-mail addresses: tarek.kandiel@kfupm.edu.sa, kandiel@science.sohag.edu.eg (Tarek.A. Kandiel).

https://doi.org/10.1016/j.apcatb.2021.121014
Received 10 September 2021; Received in revised form 15 November 2021; Accepted 12 December 2021
Available online 16 December 2021
0926-3373/© 2021 Elsevier B.V. All rights reserved.

loading with water oxidation catalyst (WOC)) were investigated to promote the PEC water oxidation process. For instance, doping with non-metal and metals dopants like P [12], Ti^{4+} [13], Sn^{4+} [14], Zr^{4+} [15] among many others has been tested to enhance the conductivity and extend the hole diffusion length. Passivating the surface states of bare hematite is also a lucrative approach for enhancing the density of photogenerated holes at the hematite surface and accelerating the water oxidation kinetics [18]. For instance, passivating hematite surface with noble metal co-catalysts (e.g. IrO_2 and RuO_2 [16,17]) exhibited a positive impact on the efficiency, but their high price and paucity prohibit their use at a large scale. Alternatively, transition metal-based materials such as Co−Pi [18,19], NiFe−layer double hydroxide (LDH) [20], phosphate ions (Pi) [21], and CoFe−Prussian Blue Analogue (CoFe−PBA)[22] were effectively utilized to decrease the surface charge recombination and hold the photogenerated holes at the surface for a time scale suitable for the water oxidation process. The ideal passivating materials/catalysts for the surface modification of hematite should have a good ability to store the photogenerated holes making them available for oxygen evolution reactions (OER) at an efficient charge transfer rate. Unfortunately, most of the passivation layers and OER catalysts cannot fulfill both criteria. Thus, the rationally designed photoanodes should be modified with interfacial layer to attract and hold the photogenerated holes at the surface and with OER catalyst to accomplish the water oxidation process at an adequate rate. Via this approach, the requirements of water oxidation process can be satisfied. Kim et al. have reported enhanced PEC activity and stable water oxidation on hematite photoanode modified with phosphate ions (Pi) [21]. They concluded that the phosphate ions anchored to the surface of hematite generate a negative electrostatic field, which stimulates the photogenerated holes separation and enhances their transfer to the surface of hematite. Moreover, Wang et al. have utilized various phosphate solutions (Na_3PO_4, Na_2HPO_4, NaH_2PO_4) to modify the hematite photoanodes and reached 0.02, 0.58, and 0.81 mA cm^{-2} at 1.23 V_{RHE}, respectively [23]. Additionally, the CoFe−PBA was also found to be an effective, robust and inexpensive electrocatalyst for water oxidation due to (i) active and stable in aqueous solutions with different pH values, from extremely acidic to extremely basic conditions; (ii) non-toxic; (iii) low overpotential for water oxidation; (iv) simple and easy to prepare [22,24,25]. Hegner et al. have modified $BiVO_4$ with CoFe−PBA co-catalyst and obtained 0.92 mA cm^{-2} at 1.23 V_{RHE} and they presented extra ordinary 50 h stability [26]. The decoration of hematite with CoFe−PBA was also investigated by the same group and they reached only 0.2 mA cm^{-2} at 1.23 $V_{RHE,}$ because the Co t_{2g} states of CoFe−PBA, which is responsible for water oxidation, is located slightly lower than the valence band (VB) edge of hematite photoanode [27]. Hence, the thermodynamic driving force to stimulate the photogenerated holes transfer from the surface of hematite to the CoFe−PBA WOC is minimal and ultimately this slow down the water oxidation kinetics. As the energy levels are not properly matched, they proposed a tunneling and hopping mechanism in the sub-band-edge states to explain the charge transfer process at the hematite/CoFe−PBA interface.

Herein, we have investigated the possibility of introducing a phosphate ions (Pi) interfacial layer on the hematite surface before loading the CoFe−PBA WOC. Via this approach, the Pi layer can drift and store the photogenerated holes at the hematite's surface and hence making them energetically accessible to transfer to the CoFe−PBA WOC and get involved in the process of water oxidation. Indeed, it is found that the existence of the Pi interfacial layer between the hematite's surface and CoFe−PBA WOC improves the photocurrent of CoFe−PBA/Pi−H photoanode at 1.23 V_{RHE} by 2.9, 1.6, and 1.9-fold relative to those of bare hematite (BH), hematite modified with only Pi layer (Pi−H), and hematite modified with only CoFe−PBA WOC (CoFe−PBA/BH), respectively. This improvement has been explained by the prolonged lifetime of the photogenerated holes, the reduced surface recombination, the anodic shift of the entire band structure, and the enhanced charge transfer efficiency as proven by transient photocurrent (TPC), intensity-modulated photocurrent spectroscopy (IMPS), Mott-Schottky (M-S) and charge separation and transfer analysis. This study provides a new approach for the rational design of hematite photoanode modified with interfacial holes drift layer and WOC for improved PEC efficiency.

2. Experimental and methods

2.1. Fabrication of bare hematite (BH) films

A β−FeOOH akaganeite film was grown on F-doped SnO_2 coated glass substrates (FTO, TEC 7, Sigma-Aldrich) by a chemical bath deposition method [28]. Briefly, the FTO substrates (1.0 × 2.0 cm^2) were cleaned and vertically immersed in a 15 mL autoclavable vial containing 5 mL of 0.15 M $FeCl_3.6H_2O$ solution. The vial was then closed and placed in a domestic oven for 6 h at 95 ℃. After cooling by quenching in a cold-water bath, the grown akaganeite films were washed with water and dried naturally in an ambient atmosphere. Then, they were heat-treated at 550 ℃ for 1 h, and calcined again at 800 ℃ for 20 min to convert the β−FeOOH akaganeite film into crystalline hematite film (denoted hereafter as BH).

2.2. Modification of hematite films with phosphate ions (Pi) layer

The BH films were immersed in 0.5 M phosphate buffer at different pH values (i.e., 4.0 – 7.0) for different durations (i.e., 30 – 120 min). Afterward, the films were withdrawn from the phosphate buffer solution and soaked in water to remove the unbound phosphate groups. Subsequently, they were dried at room temperature and calcined at various temperatures (i.e., 300 – 400 ℃) for different time intervals (i.e., 30 – 150 min) to enhance the adhesion of the anchored phosphate layer on the surface of hematite. The Pi−modified hematite films are denoted hereafter as Pi−H.

2.3. Sequential modification of Pi−H films with CoFe−PBA

The Pi−H films were further modified with CoFe−PBA WOC according to the previous report with a little modification [27]. Briefly, the Pi−H films were sequentially dipped in aqueous solutions of 20 mM $K_3[Fe(CN)_6]$ and 40 mM $CoCl_2.6H_2O$. The Pi−H films were dipped for 15 min in $K_3[Fe(CN)_6]$ solution, then they were soaked in water to remove the unbounded $K_3[Fe(CN)_6]$ and dried at room temperature. They have then dipped again for 15 min in $CoCl_2$ aqueous solution, rinsed with water, and dried. This sequence was repeated multiple times (i.e., from 2 to 8 times) for optimizing the PEC water oxidation performance. The modified Pi−H films are denoted hereafter as CoFe−PBA/Pi−H.

2.4. PEC and spectroscopic measurements

The PEC, electrochemical impedance spectroscopy (EIS), and IMPS experiments were carried out using the photoelectrochemical workstation described in ref. [28,29]. BH, Pi−H, and CoFe−PBA/Pi−H films were used as photoanodes and 1.0 M NaOH as an electrolyte. The counter and reference electrodes were Pt wire and Hg/HgO (1.0 M NaOH), respectively. Silicon reference cell (ABET technologies) was used to adjust the simulated light intensity of the 1002 SunLiteTM Solar Simulators (ABET technologies) to 1.0 sun (100 mW cm^{-2}). Eq. 1 was used to convert all measured potentials against Hg/HgO to the RHE scale ($E^{o}_{Hg/HgO}$ (1.0 M NaOH) = 0.118 V, pH = 13.6).

$$E_{RHE} = E_{Hg/HgO} + 0.059\,pH + E^{o}_{Hg/HgO} \quad (1)$$

Eq. 2 was used to calculate the applied bias photon-to-current conversion efficiency (ABPE) at different applied potentials ($V_{app.}$ vs Pt) [30]:

$$\text{ABPE}\ (\%) = \frac{j_{ph}\ (1.23 - V_b)}{P_{light}} \times 100 \quad (2)$$

where the photocurrent density (j_{ph} in mA cm^{-2}) was measured in two-electrode cell configuration under an applied bias V_b and P_{light} is the light intensity at STC (100 mW cm^{-2}).

Eq. 3 was used to calculate the incident photon-to-current conversion efficiency (IPCE) at different wavelengths (λ, nm) using a collimated and high-power LEDs (Thorlabs) [30]:

$$\text{IPCE}(\%) = \frac{1239.8\, j_{ph}}{\lambda\, P_{light}} \times 100 \quad (3)$$

The j_{ph} (mA cm^{-2}) at 1.23 V_{RHE} for BH, Pi−H, and CoFe−PBA/Pi−H were measured using a chronoamperometry technique. The light intensities of the LEDs were determined using a calibrated Si photodiode (FDS100-CAL, Thorlabs).

IMPS responses were measured at various potentials using the Autolab PGSTAT302N workstation equipped with FRA32M module, DAC164 LED driver, and Triple LED array (470 nm). This allows us to modulate the incident light and measure the modulated photocurrent responses at different frequencies (10 kHz – 0.1 Hz). Details of the setup are presented in reference [29].

The EIS experiments were executed from 100 kHz to 0.1 Hz at an amplitude of 10 mV. Mott−Schottky plots were constructed at a frequency (*f*) equal to 0.1, 1.0, or 10 kHz using a resistor and a capacitor connected in series. The space charge layer capacitance (C_{sc}) was calculated from Eq. (4).

$$\text{Im(Z)} = \frac{-1}{2\pi f C_{sc}} \quad (4)$$

From Eq. 4, the graph between log (Im(*Z*)) vs. log (*f*) gives a straight line and the slope should be equal to –1 in the pure capacitance region as seen in Fig. S1 indeed.

2.5. Real surface area (A_{real}) measurements

The A_{real} was determined from the analysis of the cyclic voltammograms (CVs) collected at different scan rates in the non-faradaic region (i.e., the region close to the open circuit potential in the dark, OCP_{dark}). Figs. S2(a-c) show the CVs of BH, Pi−H, and CoFe−PBA/Pi−H electrodes. Assuming pure capacitive current, the plot of the current vs. scan rate should give a straight line as it has been observed indeed in Fig. S2d. The slope of this straight line is equivalent to the double-layer capacitance (C_{dl}) [31]. Knowing the areal capacitance of the smooth hematite surface (i.e. 0.55 μF cm^{-2}) [32], the A_{real} and roughness factor (RF) of hematite photoanodes can be evaluated using Eqs. 5 and 6, respectively:

$$A_{\text{real}} = \frac{C_{\text{dl}}}{0.55} \quad (5)$$

$$\text{RF} = \frac{A_{\text{real}}}{A_{\text{geometrical}}} \quad (6)$$

The geometrical area ($A_{geometrical}$) is 0.25 cm^2. The A_{real} of BH, Pi−H, and CoFe−PBA/Pi−H electrodes were found to be 2.1, 2.3, and 2.4 cm^2, respectively. The RFs values for BH, Pi−H, and CoFe−PBA/Pi−H electrodes were found to be 8.4, 9.3, and 9.4, respectively.

2.6. DFT simulations

All DFT simulations have been conducted employing the Vienna ab initio simulation package (VASP [33]) as described in our previous report [28]. The slab with (001) facet was constructed with a supercell of 120-atoms 2 × 2 × 1 and 15 Å as a vacuum layer to avoid the spurious interactions between the slab and its image. The resulted dimensions of the slab were 10.22 × 10.16 dimensions in XY directions with twelve layers of thickness, six of them were fixed and six allowed to relax during the geometric optimization. The mono-protonated and mononuclear (on one iron site) structure has been used as initial geometries for the anchored phosphate/hematite complex and it is posed on an oxygen vacancy site.

3. Results and discussions

3.1. Characterization

The formation of hematite hexagonal crystal structure has been proved by analyzing the X-ray diffraction (XRD) patterns of BH, Pi−H, and CoFe−PBA/Pi−H films (Fig. 1). The characteristic diffraction peaks of (110) and (300) hematite surfaces, located at 2Θ of 35.4° and 64.0°, respectively (JCPDS card no. 033–0664), are observed. The relatively high intensity of the diffraction peak located at 35.4° in comparison with that at 64.0° indicates the preferential growth along the (110) direction. The growth of the hematite crystal along the (110) direction is beneficial for the facile electron transfer due to the high mobility of electrons in this direction [34]. The rest of the diffraction peaks are attributed to the FTO glass substrate (JCPDS card no. 041–1445). There is no significant changes have been observed in the diffraction pattern of BH upon the modification with Pi and/or CoFe−PBA evincing that the Pi and CoFe−PBA layers are very thin and beyond the detection limit of the XRD technique or they have an amorphous nature. It is worth pointing out here that the intensity of the hematite peaks is very low because the hematite films are very thin and the samples have been analyzed in the Bragg-Brentano configuration. Thus, the Raman analysis was further examined to confirm the formation of the hematite crystalline structure. As shown in Fig. S3, the prominent Raman peaks of hematite structure assigned to the E_g (243, 290, 410, and 610 cm^{-1}) and $A_{1\,g}$ (224 and 502 cm^{-1}) photon modes can be readily observed for the BH, Pi−H, and CoFe−PBA/Pi−H films [35,36].

The morphologies of the β−FeOOH, BH, Pi−H, and CoFe−PBA/Pi−H films have been investigated by SEM and presented in Fig. 2 micrographs a–d, respectively. The analysis of the SEM micrographs indicated that the β−FeOOH film consists of a compact layer of nanorods with a diameter of approx. 50 nm (Fig. 2a). After calcination, rod-like particles have been formed and their diameters increased up to 100 nm (Fig. 2b). After the modification of the BH films with either Pi and/or CoFe−PBA, their morphologies remain the same evincing that the deposited Pi and/or CoFe−PBA layers are very thin and beyond the resolution of the SEM techniques. However, the energy-dispersive X-ray spectroscopy (EDXS) spectra shown in Figs. S4−6 confirmed the existence of P, Co, C, and N in

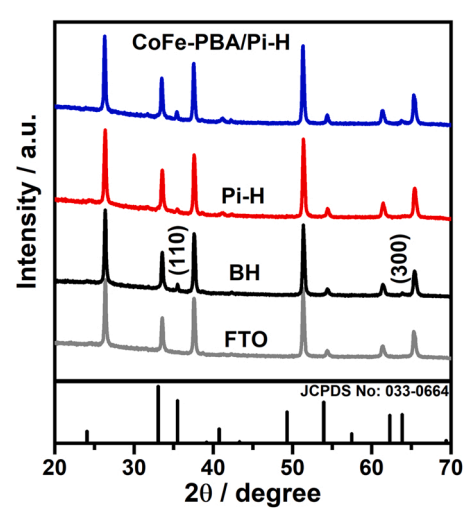

Fig. 1. Bragg-Brentano XRD diffraction pattern of FTO, BH, Pi−H, and CoFe−PBA/Pi−H films. The vertical lines indicate the Bragg positions for hematite crystal structure (JCPDS card no. 033–0664).

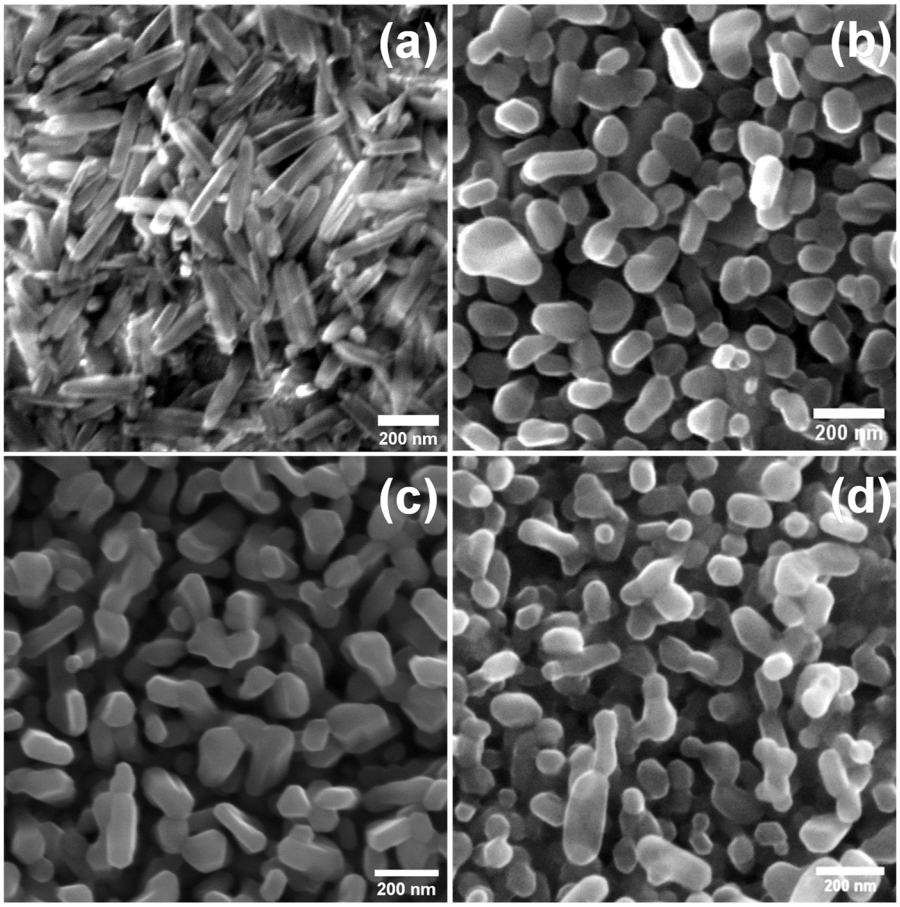

Fig. 2. SEM micrographs of as-grown β−FeOOH akaganeite (a), bare hematite (BH, b), Pi−modified hematite (Pi−H, c), and CoFe−Prussian blue analogue/Pi−modified hematite films (CoFe−PBA/Pi−H, d).

the modified hematite films. The high-intensity peaks of Sn and Si originate from the conductive F-doped SnO_2 layer coated on the FTO substrate.

To prove the existence of Pi and CoFe−PBA on the hematite's surface, the XPS spectra of BH, Pi−H, and CoFe−PBA/Pi−H films have been measured and analyzed. Fig. S7 illustrates the low-resolution XPS survey spectra, which confirm the existence of P 2p in the Pi−H film and P 2p and N 1s core-levels in the CoFe−PBA/Pi−H film. None of them can be observed in the BH film, which indicates the successful modification of BH with Pi and CoFe−PBA/Pi layers. Fig. 3a presents the high-resolution XPS (HR-XPS) spectra of the P 2p core-level. The characteristic XPS peak of P 2p located at 133.7 eV can be only found in the Pi−H and CoFe−PBA/Pi−H films confirming that the phosphate group is well anchored to the hematite surface [21]. For the BH film, the two XPS peaks located at ~710.6 and ~724.0 eV and separated by approx. 13.4 eV (i.e., spin-orbit splitting energy, ΔE) can be assigned to Fe $2p_{3/2}$ and $2p_{1/2}$, respectively. These two peaks confirm the presence of iron in the oxidation state of + 3 (Fig. 3b) [37]. The little shift towards lower binding energy observed after the modification with CoFe−PBA indicates the coexistence of iron + 2 in the CoFe−PBA layer [27]. The HR-XPS spectrum of Co 2p core levels in the CoFe−PBA/Pi−H film is shown in Fig. 3c. A broad XPS spectrum was observed more likely due to the overlap of the XPS spectra of the mixed oxidation state of Co (i.e., oxidation states +2 and +3) in the CoFe−PBA layer [38]. It was not possible to make reasonable deconvolution of the overlapped peaks due to the low intensity of the signal. To confirm further the coexistence of the mixed oxidation states of cobalt, the CoFe−PBA power was prepared and isolated under the same conditions as for the modification of hematite film, and the XPS spectrum was measured and presented in Fig. S8. The analysis of the XPS spectrum of the isolated CoFe−PBA powder confirms the coexistence of Co in the oxidation state + 2 and + 3. The presence of CoO_x has been excluded due to the absence of the CoO_x characteristic peaks at 780 eV. This confirms that Co ions are mainly bound with cyanide ions in the matrix or partly to the oxygen of water and not with oxygen to form CoO_x [27]. The presence of N 1s XPS peak at 399.3 eV as shown in Fig. 3d can be assigned to the nitrogen in cyanide ions [26,27]. The HR-XPS spectra of O 1s core levels in BH and Pi−H films are shown in Fig. 3e. They can be de-convoluted into three peaks corresponding to the different oxygen species (Fig. 3f for Pi−H film and Fig. S9 for BH film). In Fig. 3f, the peak located at ~ 529.8 eV belongs to the lattice oxygen bond (O^{2-}), while the peaks located at ~ 531.5 and ~ 532.3 eV are the oxygen vacancies and surface adsorbed oxygen species, respectively [39,40]. The oxygen vacancies (defected oxygen sites), that might be resulted from the defects in the surface bounded phosphate ion layer, modify the coordination of O atoms and the chemical valence of Fe atoms, and thus they change the O−Fe bonds and alter the XPS spectrum of the O 1s as previously reported [40]. The areas under the three de-convoluted peaks was analyzed and tabulated (Table S1). They revealed that the surface of hematite is enriched with oxygen vacancies (defect sites) after its modification with the Pi layer. It seems that the modification of the hematite with phosphate ions induces the formation of defect sites. Moreover, the binding energy of O 1s in Pi–H was slightly lower than that in BH, implying that the anchored phosphate ions change the surface electronic properties of bare hematite [21]. On realistic surfaces of hematite, different kinds of surface defects are exist and they play different roles. It was reported that some of them have a positive impact on the PEC water oxidation (i.e., facilitating the water oxidation process), but the rest lead to severe interfacial

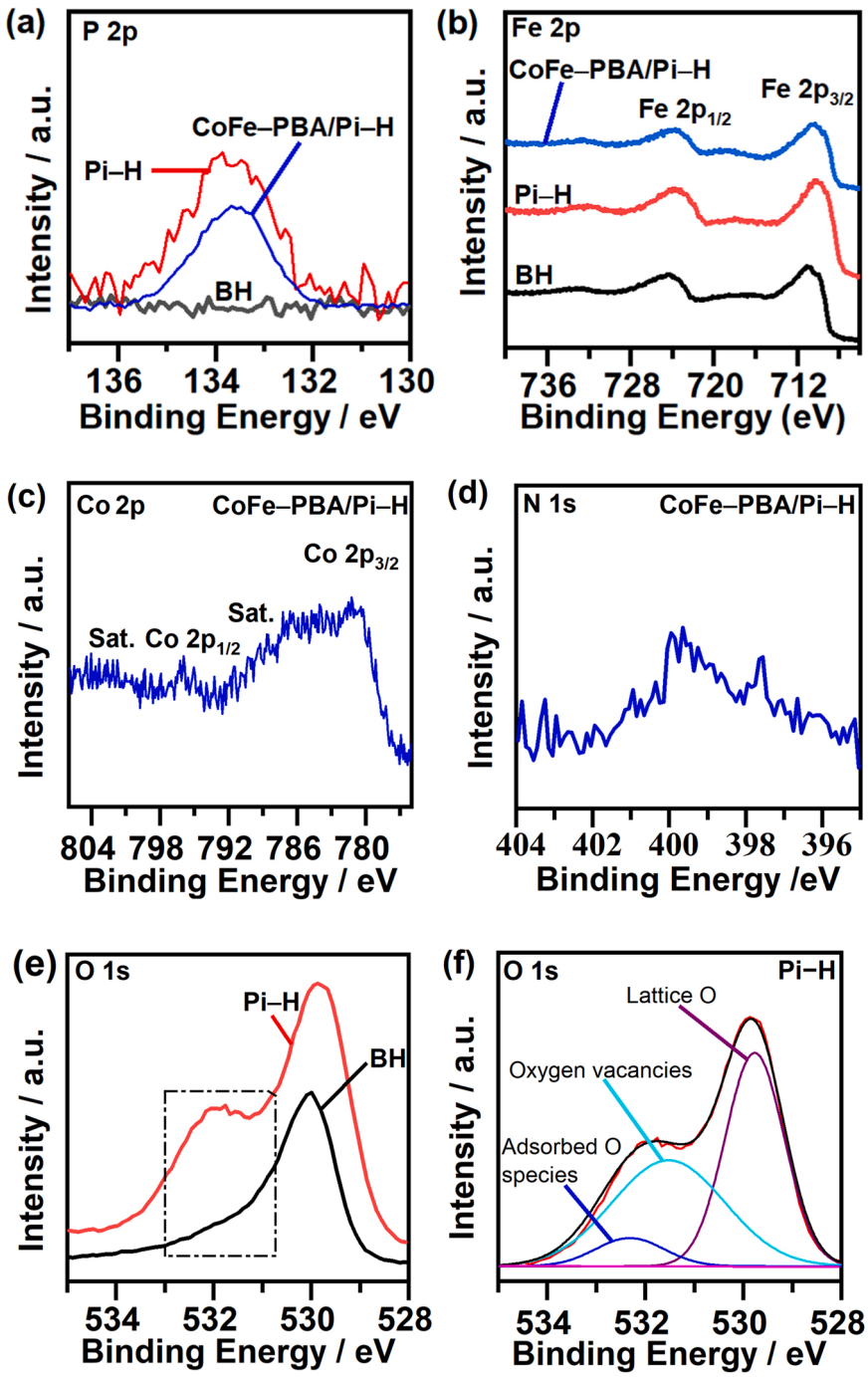

Fig. 3. HR-XPS spectra of P 2p (a), Fe 2p (b), Co 2p (c), N 1s (d), and O 1s (e, f) core-levels in BH, Pi−H and CoFe−PBA/Pi−H films.

recombination at the semiconductor/electrolyte (S-E) interface [40,41].

3.2. Modification and PEC measurements

The detailed PEC performance of bare and modified hematite photoanodes was assessed in an aqueous solution of 1.0 M NaOH under STC (i.e., 1.0 sun, AM 1.5 G). Linear sweep voltammetry (LSV) and chronoamperometry (CA) procedures were used to measure the continuous and chopped photocurrent. Based on the pH value, the surface hydroxyl groups of hematite, as a metal oxide, can be either protonated (positively charged) or deprotonated (negatively charged) when dipped in an aqueous solution. At a pH value equal to the point of zero charge (pH_{PZC}), the surface of hematite will remain un-charged. For instance, it is reported that the surface of hematite will remain un-charged in the pH range from 7 to 9.5 (i.e., at pH values equal to the point of zero charge) [42]. Thus, at pH less than the pH_{PZC}, the surface of hematite will maintain a positive charge, and hence the electrostatic adsorption of PO_4^{3-} ions (Pi) is favorable. Elzinga and Sparks [43] have used ATR-FTIR spectroscopy to examine the adsorption of phosphate ions on the surface of hematite at a wide range of pH values. They found that the pH value greatly affects the adsorption process and different phosphate complexes can exist on the surface of hematite, but the formation of mono-protonated phosphate species bound in a monodentate bridging fashion is favored in the pH range from 3.5 to 7.0. To define the optimum pH value for anchoring the Pi onto the surface of hematite via adsorption, the BH films were first immersed for different time intervals

(i.e., 30 – 120 min) at different pH values (i.e., pH 4.0 – 7.0) in phosphate aqueous solutions. After the adsorption step, the films were washed with de-ionized water to remove the unattached phosphate ions, subsequently, the modified hematite films were calcined at various temperatures (i.e., 300–400 ℃) for different time intervals (i.e., 30 – 150 min) to improve the adhesion of the Pi layer. Figs. S10, S11, S12, and S13 illustrate the photocurrent responses of the fabricated Pi–H photoanodes at different aforementioned conditions. It was found that the Pi−H photoanode fabricated by dipping in 0.5 M phosphate buffer for 60 min at pH 5.8 and subsequently annealed at 350 ℃ for 1.0 h exhibits the highest PEC activity. The Pi−H was further modified with CoFe−PBA OEC using a sequential dipping method. The Pi−H electrode was dipped in 0.02 M $K_3[Fe(CN)_6]$ aqueous solutions for 15 min followed by immersing in 0.04 M $CoCl_2$ aqueous solution for 15 min. Repeating this process for 4 cycles produces the highest PEC activity (see Fig. S14). The Pi−H photoanode exhibits 0.78 mA cm^{-2} at 1.23 V_{RHE} under STC, which is 1.8 −fold greater than that of BH photoanode (0.43 mA cm^{-2}) and consistent with the previously reported values [23]. Interestingly, the co-modification of BH with Pi layer and CoFe−PBA OEC enhance the photocurrent by 2.9 −fold to reach 1.24 mA cm^{-2} at 1.23 V_{RHE} as shown in Fig. 4a. This value is 6 −fold higher than the value reported for the hematite photoanode modified with only CoFe−PBA OEC (i.e., 0.2 mA cm^{-2}) [27]. It is worth mentioning that it was not possible to reach this value of photocurrent by the simple modification of the BH photoanode with only Pi or CoFe−PBA OEC layer evincing that the Pi interfacial layer between hematite surface and CoFe−PBA OEC plays a crucial role. The Pi layer between CoFe−PBA and BH provides a new path to drift and store the photogenerated holes making them energetically accessible for water oxidation via the CoFe−PBA OEC. Fig. 4b depicts the photo-conversion efficiency as a function of applied potentials for BH, Pi−H, and CoFe−PBA/Pi−H photoanodes. The maximum ABPE of CoFe−PBA/Pi−H photoanodes reaches 0.70% at 0.37 V_{Pt}, which is 1.4 and 3 −time higher than that of Pi−H (i.e., 0.50% at 0.41 V_{Pt}) and BH (i.e., 0.24% at 0.57 V_{Pt}), respectively. Moreover, the potential at the maximum ABPE for the CoFe−PBA/Pi−H photoanode is shifted cathodically by 200 mV in comparison with that of BH which can be attributed to the reduced surface recombination at semiconductor/electrolyte interface (SEI) and the enhanced photovoltage (discussed later). The PEC stability of CoFe−PBA/Pi−H photoanode was investigated by applying a constant bias potential (i.e., 1.23 V_{RHE} at pH = 13.6) for 15 h (Fig. 4c). The fluctuations of the obtained photocurrent were as low as 4%, proving that the CoFe−PBA/Pi−H photoanode exhibits high stability. The photocurrent improvement was further verified by measuring the IPCE as a function of the incident photons wavelength. The IPCE of BH, Pi−H, and CoFe−PBA/Pi−H photoanodes measured at 1.23 V_{RHE} are demonstrated in Fig. 4d. In agreement with the LSV curves presented in Fig. 4a, the CoFe−PBA/Pi−H photoanode exhibits the highest IPCE (i.e., 35.1% at 430 nm). To confirm that the photocurrent improvement is due to the surface modification of hematite photoanode with Pi layer and CoFe−PBA OEC and not due to the difference in the light absorption capability, the optical properties of the BH, Pi−H, and CoFe−PBA/Pi−H photoanodes have been measured. The bare and modified hematite photoanodes showed almost the same light absorption properties and bandgap (Fig. S15a and b). This implies that the PEC improvement is mainly due to the surface modification with Pi layer and CoFe−PBA OEC indeed.

The influence of Pi layer and CoFe−PBA OEC on the transient decay

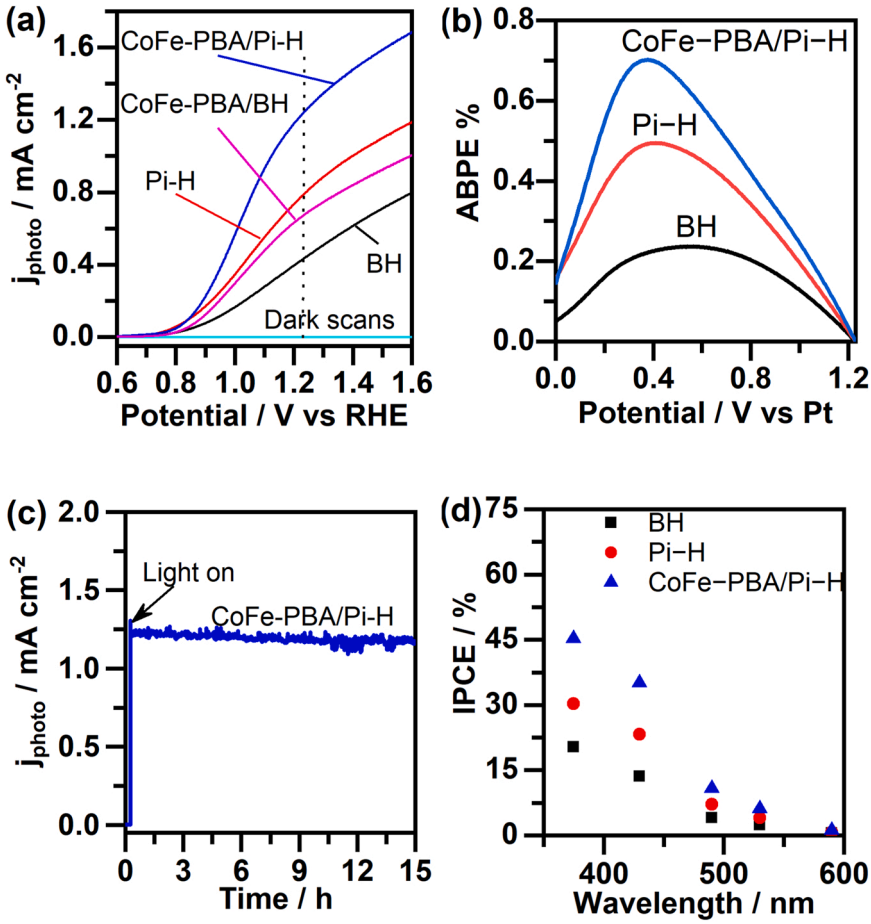

Fig. 4. (a) LSV curves and (b) ABPE % of BH, Pi−H, CoFe−PBA/BH and CoFe−PBA/Pi−H photoanodes, respectively; (c) Long-term stability test of CoFe−PBA/Pi−H photoanode measured at 1.23 V_{RHE}; (d) IPCE % of BH, Pi−H and CoFe−PBA/Pi−H photoanodes.

time of the photogenerated holes has been examined. In agreement with the earlier reports, anodic and cathodic spikes are observed in the transient photocurrent (TPC) responses as shown in Fig. 5a [5,44]. Briefly, when the light is turned on, an anodic photocurrent spike (I_m) is usually observed due to the movement of the photogenerated holes towards the SEI where they are accumulated at the surface trapping states due to the slow kinetics of water oxidation. During continuous illumination, the steady-state current (I_s) is established, where the arrival of holes concentration is balanced by the holes recombination and transfer for OER. The area under the anodic spike peak is proportional to the amount of the surface trapped holes. These areas were calculated by integration and found to be 8.43 ± 0.78, 11.26 ± 0.35, 7.51 ± 0.14, and 5.22 ± 0.21 μC cm^{-2} for BH, Pi−H, CoFe−PBA/BH, and CoFe−PBA/Pi−H photoanodes, respectively. The amount of the accumulated holes in Pi−H is significantly higher than that of BH indicating that the Pi layer acts as a hole accumulation layer. Moreover, the photocurrent spike of Pi−H is much higher than that of BH indicating that the Pi layer facilitates the drift of the photogenerated holes toward the SEI. The concentration of accumulated holes and the photocurrent spike are then reduced upon the modification with CoFe−PBA OEC. This can be attributed to the passivation of the surface states by CoFe−PBA and the transfer of the photogenerated holes to the CoFe−PBA OEC where they partake in the water oxidation process. Once the light is off, the conduction band electrons recombine with the surface trapped holes to give a cathodic current spike [44]. It was noted that the cathodic current spike of Pi−H is more significant than those of BH, CoFe−PBA/BH, and CoFe−PBA/Pi−H photoanodes indicating again that the Pi−H exhibits a higher amount of surface trapped holes evincing that the Pi layer is indeed accumulating the holes at the surface of hematite photoanode. To get more insights, the transient decay time (τ) was further calculated. τ is defined as the time at which ln(D) = −1 and the D parameter is determined by using Eq. (7):[45].

$$D = (I_t - I_s) / (I_m - I_s) \tag{7}$$

Where I_t is time-dependent current, I_m is photocurrent spike, and I_s is the steady-state current as illustrated in Fig. 5a. The normalized D value plotted versus time is presented in Fig. 5b. The τ values of BH, Pi−H, CoFe−PBA/Pi−H, and CoFe−PBA/Pi−H photoanodes were estimated to be 45, 37, 58, and 86 ms, respectively. Generally, a slower recombination rate will lead to a higher τ value [46]. The significantly high transient decay time of CoFe−PBA/Pi−H relative to those of Pi−H and CoFe−PBA/BH indicates that the synergy between Pi layer and CoFe−PBA OEC has a positive impact on the charge separation efficiency. The transfer of the accumulated holes at the Pi layer to the CoFe−PBA OEC makes them available for a longer time at the surface, and thus, they can be readily involved in the water oxidation process. In absence of CoFe−PBA, the Pi−H photoanode exhibits the highest amount of surface trapped holes, however, their shorter lifetime limits the PEC efficiency. It seems that the defects induced by the Pi layer on the hematite surface drift the photogenerated holes toward the surface, but their surface recombination with the conduction band electrons dominates the process and limits the water oxidation process. Fig. S16 shows the LSV of BH, Pi−H, and CoFe−PBA/Pi−H photoanodes measured under chopped light. It is observed that with increasing the applied potential, the anodic spikes are diminished indicating that the applied positive bias suppresses the electron concentration at the surface and evacuates the surface states. At relatively low bias potential, the comparison of the anodic and cathodic spikes revealed that the anodic and cathodic peaks are less for the CoFe−PBA/Pi−H than Pi−H and BH. This again indicates in general that the CoFe−PBA suppresses the surface recombination by passivating the surface defects and accelerates the holes injection into the solution for the water oxidation process.

The enhanced PEC performance of the CoFe−PBA/Pi−H photoanode was further verified by measuring the generated photovoltage (V_{ph}). The V_{ph} was calculated from the difference between the light and dark open-circuit potentials ($OCP_{light} - OCP_{dark}$). Fig. 6a illustrates the cathodic shift of the OCP under illumination which is a characteristic property of the n-type material [21]. The results indicated that the V_{ph} of CoFe−PBA/Pi−H (i.e., 0.24 V) is higher than those of Pi−H (i.e., 0.18 V) and BH (i.e., 0.14 V) photoanodes, which indicates that the CoFe−PBA passivate the surface defects and reduces the surface recombination [47]. Besides, the surface modification of BH with Pi interfacial layer and/or CoFe−PBA OEC might affect the electrochemical surface area (ECSA) and hence the PEC activity. To investigate this assumption, the ECSA has been measured (Fig. S2). It was found that the BH, Pi−H, and CoFe−PBA/Pi−H photoanodes exhibit approximately the same ECSA and thus the ECSA has an insignificant influence on the PEC activities of the investigated photoanodes.

3.3. EIS and IMPS measurements

The effect of Pi layer on the flat band potential and the donor density of the fabricated hematite electrodes have been investigated by EIS. Fig. 6b shows the Mott−Schottky (M−S) plots of BH, Pi−H, and CoFe−PBA/Pi−H electrodes constructed at 1.0 kHz using Eq. (8) [28]:

$$\frac{1}{C_{SC}^2} = \frac{2}{q\varepsilon\varepsilon_0 A^2 N_d}\left(E - E_{fb} - \frac{kT}{q}\right) \tag{8}$$

where each term in this equation has its general meaning as described in ref. [28]. All electrodes exhibit a straight line with a positive slope,

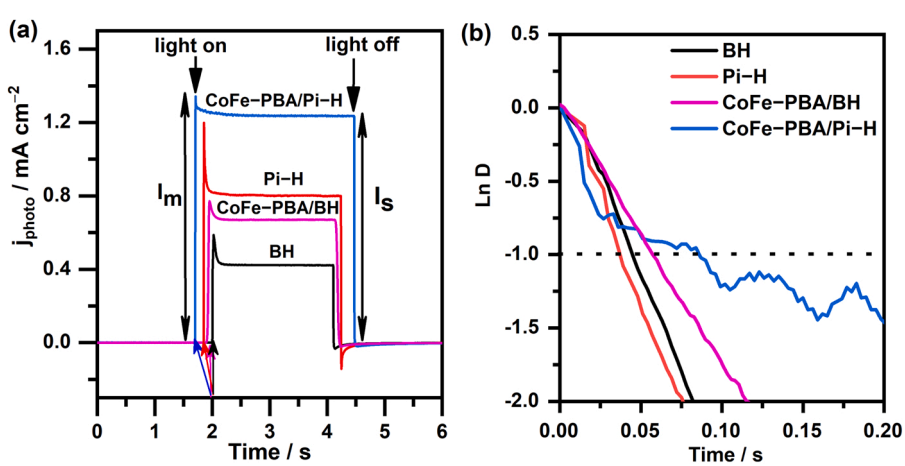

Fig. 5. (a) Transient photocurrent (TPC) response and (b) Anodic transient decay times for BH, Pi−H, CoFe−PBA/BH, and CoFe−PBA/Pi−H measured at 1.23 V_{RHE} under STC (1.0 sun, AM 1.5 G).

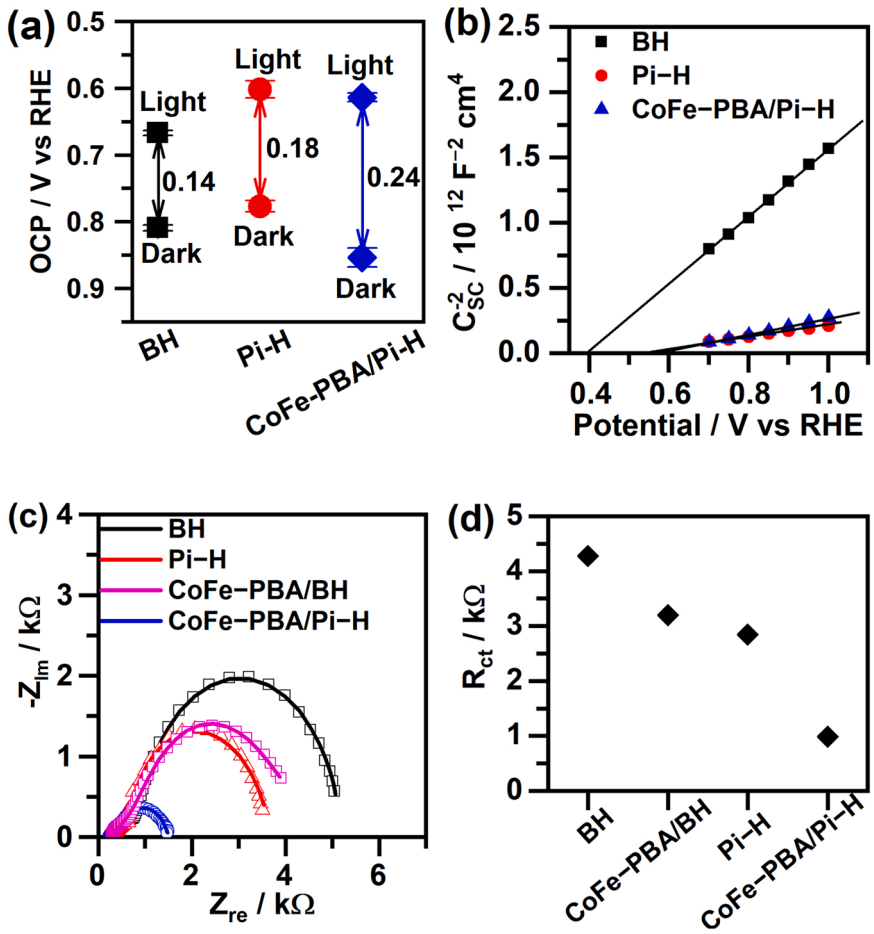

Fig. 6. (a) Open circuit potential (OCP), and (b) Mott–Schottky plots of BH, Pi–H, and CoFe–PBA/Pi–H photoanodes at 1.0 kHz. (c) Nyquist plots and (d) R_{ct} of BH, Pi–H, CoFe–PBA/BH, and CoFe–PBA/Pi–H photoanodes measured at 0.9 V_{RHE} under STC (1.0 sun, AM 1.5 G).

which divulged that all of them are n-type materials with electrons are the majority charge carriers. Fig. S17 (a–c) displays the M–S plots of BH, Pi–H, and CoFe–PBA/Pi–H measured at 0.1 and 10 kHz which show the same trend as that measured at 1.0 kHz but having a different slopes. The difference in the slopes is commonly encountered and usually attributed to the dispersion of the measured capacitances because of the roughness of the electrode surface [28,48]. The M–S plot recorded at 1.0 kHz has been used to calculate the donor density for ease of comparison with the literature. The donor densities have been derived from the slopes acquired from the linear regression fitting according to the M–S equation and presented in Table S2. It was found that the donor density of Pi–H is increased by approximately 5 –fold, i.e., from 1.54×10^{17} cm^{-3} for BH to 8.12×10^{17} cm^{-3}, which indicates that the phosphate ions create defects on the surface of hematite and induce more oxygen vacancies. This finding is consistent with the XPS and TPC results. The flat band potential (E_{fb}) has been determined from the intercept of the M–S plot with the x – axis at C_{SC}^{-2} equal to zero and it was found to be approximately 0.37 V_{RHE} for BH. The E_{fb} of Pi–H and CoFe–PBA/Pi–H electrodes were found to be 0.52 and 0.55 V_{RHE}, respectively. The OCP_{light} can be used to verify the E_{fb} provided that the material does not have very fast surface recombination [30]. Indeed, the determined E_{fb} for Pi–H and CoFe–PBA/Pi–H electrodes are consistent with the measured OCP_{light} (i.e. 0.60 V_{RHE} for Pi–H and 0.61 V_{RHE} for CoFe–PBA/Pi–H) evincing the reliability of the results. For the BH electrode, the OCP_{light} (i.e. 0.67 V_{RHE}) is more anodic than the true E_{fb} due to the high rate of carriers recombination. This behavior is expected for n-type semiconductors [30]. Despite the anodic shift of the flat band potential of the CoFe–PBA/Pi–H photoanode relative to that of BH, it exhibits higher PEC activity at a lower bias potential. It is important to mention here that the Co t_{2g} hole-acceptor states of CoFe–PBA are located slightly at lower energy than the valence band (VB) edge of hematite [27]. Thus, there is no driving force for the hole to be transferred from the VB of hematite to the CoFe–PBA OEC. Since the bandgaps of BH, Pi-H, and CoFe-PBA/Pi-H electrodes are the same (Fig. S15), the anodic shift of the flat band potential observed after the modification with Pi layer will result in a shift of the valance band edge in the same direction. Consequently, the VB edge of hematite will be shifted to a lower energy level than that of the Co t_{2g} hole-acceptor states and thus the hole transfer from the VB of hematite to the CoFe–PBA will be energetically more favorable. However, this information along with the enhanced V_{ph} indicates that the synergy between the Pi interfacial layer and the CoFe–PBA OEC suppresses the surface recombination and facilitates the charge transfer, no significant cathodic shift in the onset potential. This is because the energy level of the Co t_{2g} hole-acceptor states in CoFe-PBA are fairly close to the VB edge of BH and the entire band structure of hematite is shifted anodically after modification. Since the electric field within the space charge layer is the main driving force for the separation of the electron/hole pairs, only the generated charge carriers within the range of (L_p+ W) can reach the SEI (where L_p is the hole diffusion length and W is the depletion layer width). Because of the short hole diffusion length of hematite (2–3 nm), there is still a high probability for recombination within the space charge layer. Thus reducing the width of the space charge layer might still reduce the surface recombination and enhance the PEC activity assuming that a significant portion of the light is absorbed within the space charge layer [49,50]. The W of BH, Pi–H, and CoFe–PBA/Pi–H photoanodes has

thus been calculated using equation Eq. (9) [29]:

$$W = \sqrt{\frac{2\varepsilon\varepsilon_0(E_{app} - E_{FB})}{qN_d}} \quad (9)$$

where E_{app} and E_{FB} denote the applied and flat band potentials, respectively. The depletion layer widths of BH, Pi−H, and CoFe−PBA/Pi−H at 1.23 V_{RHE} are 26.4, 8.9, and 11.8 nm, respectively. The decreased depletion layer width for Pi−H and CoFe−PBA/Pi−H relative to that of BH will shorten the charge collection distance [49,50]. Thus, more holes can be drifted toward the SEI and have a higher probability to participate in the water oxidation process at the CoFe−PBA OEC. The Nyquist spectra measured at 0.9 V_{RHE} and presented in Fig. 6c confirmed that the CoFe−PBA OEC facilitates the water oxidation process more efficiently in presence of Pi layer. As shown in Fig. 6c, the size of the low frequency (LF) semicircle, which corresponds to the impedance events at the SEI, particularly the charge transfer resistance R_{ct}, is significantly decreased after the modification of Pi-H photoanode with CoFe−PBA OEC. By fitting the Nyquist spectra to the equivalent circuit presented in Fig. S18, the R_{ct} has been calculated and presented in Fig. 6d. However, the modification of BH with Pi layer or CoFe−PBA OEC reduces to some extent the R_{ct} value, none of them were able to reach the R_{ct} value of the CoFe−PBA/Pi−H photoanode. These results indicate that the Pi interfacial layer is essential to extract the photogenerated holes from the light-harvesting hematite photoanode and transfer them to the CoFe−PBA OEC. This step is very important to reduce the surface recombination and accelerate the kinetics (holes transfer) for the water oxidation process.

The synergy between Pi layer and CoFe−PBA OEC and their influence on the charge transfer efficiency has further been examined by the IMPS technique. Fig. S19 illustrates the typical IMPS response for BH photoanode measured at 1.0 V_{RHE}. It consists of two semicircles located at the first and fourth quadrants. The HF semicircle starts from the fourth quadrant and represents the RC time constant of the cell, which comprises the total resistance of the cell and combined capacitance of the space charge layer and Helmholtz layer capacitance. The LF semicircle appears in the first quadrant, where the charge transfer process and surface recombination dominate. The phenomenological rate constants of charge transfer (k_{tr}) and charge recombination (k_{rec}) at different bias potentials can be obtained by analyzing the positive/positive part of the IMPS spectra as shown in Fig. 7(a−c). The LF intercept is related to the surface charge transfer efficiency (η_{ct}) and equal to k_{tr} / (k_{tr} + k_{rec}), whereas $\omega_{max} = 2\pi f_{max} = k_{tr} + k_{rec}$ [51–53]. Then, k_{tr} and k_{rec} can be calculated at various potentials from the low-frequency intercept and ω_{max} for BH, Pi−H, and CoFe−PBA/Pi−H photoanodes. Fig. 8(a and b) shows the calculated k_{rec} and k_{tr} of BH, Pi−H, and CoFe−PBA/Pi−H photoanodes at various potentials. It is observed that across the entire potential window the k_{tr} increases in the following order: k_{tr} (CoFe−PBA/Pi−H) > k_{tr} (Pi−H) > k_{tr} (BH) which is consistent with the LSV and EIS results. Surprisingly, the k_{rec} of Pi−H is higher than that of BH photoanode despite the latter exhibiting lower PEC activity. This can be understood by considering that the accumulation of holes in the Pi layer facilitates, to a certain extent, the charge transfer kinetics at the SEI, but also increases the rate of recombination is consistent with the TPC results (Fig. 5b). The reduced k_{rec} of Pi−H photoanode after modification with CoFe−PBA confirms that the CoFe−PBA OEC suppresses the surface recombination, more probably by passivating the defect sites, and enhances the charge transfer kinetics and ultimately the PEC water oxidation activity. The charge-transfer efficiencies (η_{ct}) of BH, Pi−H, and CoFe−PBA/Pi−H have been calculated according to Eq. (10) and presented in Fig. 8c. The trends of η_{ct} are consistent with the *I*−*V* curves presented in Fig. 4a.

$$\eta_{ct}\,(\%) = k_{tr} \times 100 / (k_{tr} + k_{rec}) \quad (10)$$

The efficiencies of charge separation (η_{sep}) and charge transfer (η_{cat}) which represent the complete utilization of the surface holes by Na_2SO_3 electron donors and the surface hole injections, respectively, have been calculated according to the previous report [54]. Fig. 9a shows the solar photocurrent calculated by considering the fractions of light absorbed at different wavelengths under AM 1.5 G illumination. The integrated values of the solar photocurrent (J_{abs}) are also presented in Fig. 9a. The j-V curves of BH, Pi−H, and CoFe−PBA/Pi−H photoanodes measured in an aqueous solution of NaOH with and without Na_2SO_3 are shown in Fig. 9b. The η_{sep} and η_{cat} are defined as the ratios of j_{photo}/J_{abs} and $j_{photo}/j_{photo}(Na_2SO_3)$, respectively, and presented in Fig. 9c and d, respectively. Low η_{sep} values were observed for BH through the entire potential window due to the high rate of bulk and surface recombination. The modification of BH with Pi layer has a little impact on the η_{sep} indicating that Pi alone is not adequate to suppress the recombination and improve the charge separation efficiency in agreement with the TPC and IMPS results. Upon the modification with CoFe−PBA, a significant improvement has been observed evincing that CoFe−PBA is important to suppress the surface recombination, passivate the surface defects, and accelerate the hole injection. The η_{sep} of CoFe−PBA/Pi−H at 1.23 V_{RHE} (i.e. 23.4%) is improved by a factor of 3.1 and 2.2-fold relative to those of BH (7.5%) and Pi-H (10.7%), respectively. The η_{cat} of CoFe−PBA/Pi−H at 1.23 V_{RHE} is also enhanced by 36% and 8.5% relative to those of BH and Pi−H, respectively. It is also notable here that the η_{cat} of Pi−H is enhanced by 12.6% relative to that of BH at 1.23 V_{RHE}. This indicated that surface defects (oxygen vacancies) created by the Pi layer on the surface of hematite have a positive impact on water oxidation, but they still cannot efficiently suppress the surface recombination. In general, the η_{sep} and η_{cat} results indicated that CoFe−PBA has a dual function. It passivates the surface states and enhances the separation efficiency and at the same time improves the hole injection and accelerates the water oxidation kinetics.

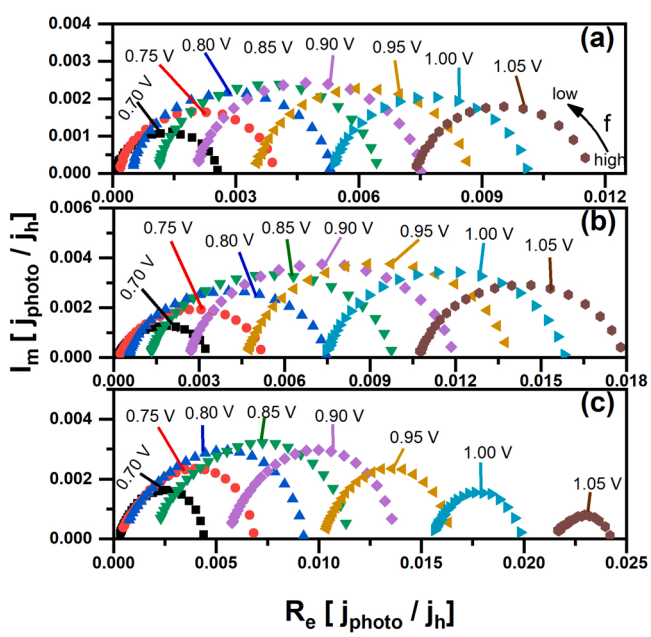

Fig. 7. IMPS responses of BH (a), Pi−H (b), and CoFe−PBA/Pi−H (c) electrodes as a function of the applied potentials.

3.4. DFT simulation

DFT simulations have been conducted to further explore the effect of the phosphate ion (Pi) layer on the electrostatic potential of the hematite surface. The change of the surface electrostatic potential could influence the diffusion of the photogenerated holes toward the surface and thus affects the PEC catalytic activity as observed in this study and supported

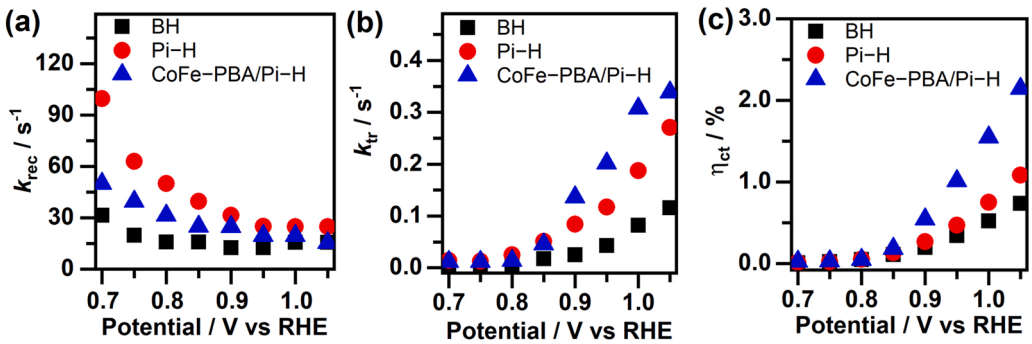

Fig. 8. Apparent rate constants of charge recombination (k_{rec}, a) and transfer (k_{tr}, b), and charge transfer efficiency (η_{ct} %, c) of BH, Pi−H, and CoFe−PBA/Pi−H electrodes as a function of the applied potentials.

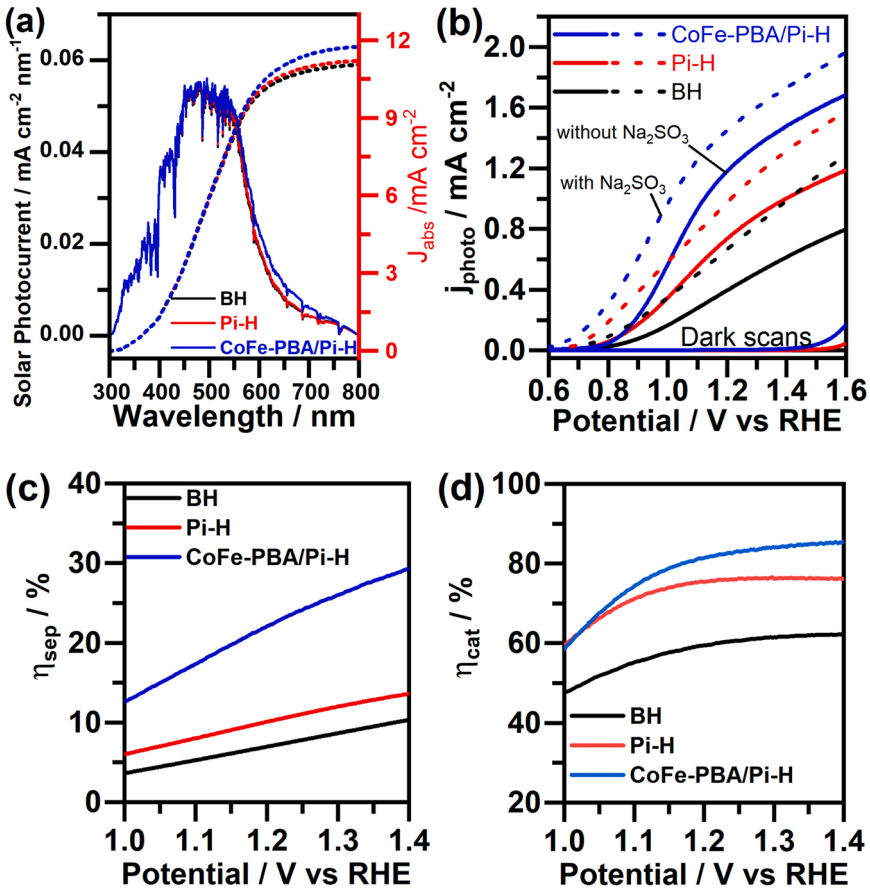

Fig. 9. (a) Solar and integrated photocurrent densities, (b) j-V curves measured in an aqueous solution of NaOH with (dashed line) and without (solid lines) Na_2SO_3, (c) Charge separation efficiency (η_{sep}), and (d) charge transfer efficiency (η_{cat}) of BH, Pi−H, and CoFe−PBA/Pi−H photoanodes.

by TPC and IMPS results.

Our previous report showed that the (001) surface is more stable than (110) [28]; therefore, we focused here only on the (001) facet. Based on the ATR-FTIR spectroscopy study of the adsorption of phosphate ions on hematite's surface [43], the mono-protonated mononuclear form is the dominant species. Therefore, we have modeled this form as the initial geometry for the adsorbed phosphate/hematite complex and posed it on an oxygen vacancy site. Results in Fig. 10 showed that the deposition of Pi layer on the BH surface induced a drift on the BH's surface electrostatic potential toward more negative potential in agreement with the previous report [21]. Such a drift in the electrostatic potential is beneficial for the water oxidation reactions as it makes the diffusion of the photogenerated holes toward the surface easier than in BH. It would also favor the formations of more oxygen-deficient vacancies (i.e., +1, +2 states). The defect stabilization comes from the strong electrostatic attraction between the positively charged states and the Pi surface layer.

Based on the photoelectrochemical and the DFT calculation results, the roles of Pi interfacial layer and CoFe−PBA OEC are schematically illustrated in Scheme 1. In the case of BH photoanode (Scheme 1a), most of the photogenerated holes recombine within the bulk and few of them can be separated by the electrical field within the space charge layer. Since the L_p of hematite is too short (2−3 nm), serious recombination takes place in the space charge layer in addition to recombination at the surface states. In addition, since the energy level of the Co t_{2g} hole-acceptor states in CoFe−PBA are below the VB edge of hematite [27],

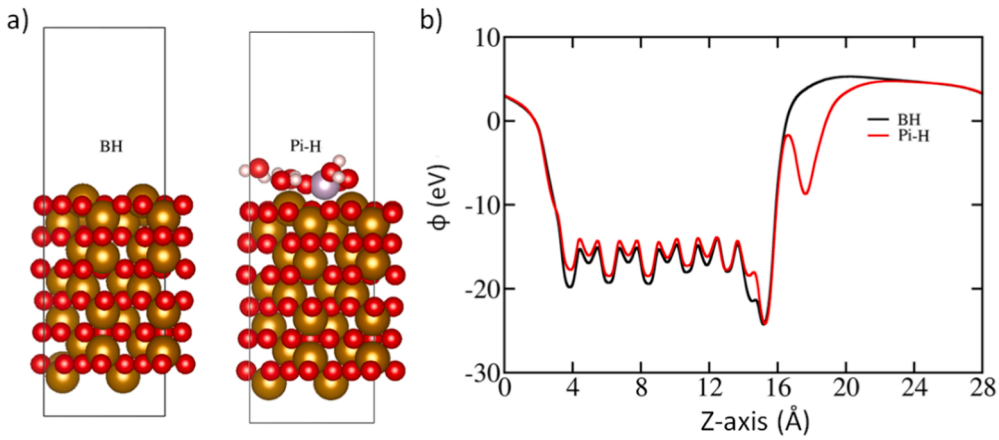

Fig. 10. DFT slab models used for the electrostatic potential calculations. a) Hematite (001) slabs of clean surface and with phosphate ion (color code: O: red, H: white, Fe: light brown, P: plum). b) The electrostatic potential (eV) of BH and Pi−H slabs.

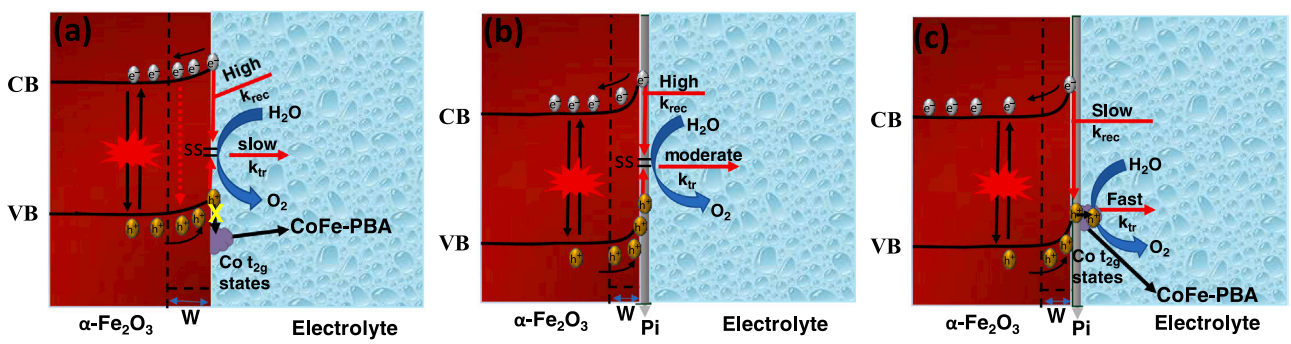

Scheme 1. Energetic schemes for (a) BH, (b) Pi−H and (c) CoFe−PBA/Pi−H illustrate surface recombination rate (k_{rec}) and charge transfer rate (k_{tr}) at the hematite/Pi/CoFe-PBA interfaces. SS represents the surface states.

there is no driving force for the hole transfer from the VB edge of hematite to the CoFe−PBA. Thus, the modification of hematite with CoFe−PBA only will not significantly improve its PEC activity as observed in this study indeed. The modification of hematite with Pi layer facilitates the drift of photogenerated holes toward the surface and reduces the width of the depletion layer and shortens the charge collection distance [49,50], thus increasing the concentration of holes at the surface. It also shifts the entire band structure anodically and thus better energy band alignment is achieved between the energy level of Co t_{2g} hole-acceptor states in CoFe-PBA and the VB edge of hematite. In the absence of OEC (Scheme 1b), the holes are accumulated in the Pi layer at the defect sites which can catalyze the water oxidation but, at the same time, induce severe interfacial recombination at the semiconductor/electrolyte (S-E) interface via the surface states. Thus, only a small fraction of them can transfer to the electrolyte and oxidize water and the rest recombine with the conduction band's electrons via surface states. The addition of the CoFe−PBA OEC to the Pi−H surface will passivate the surface states and reduce the surface recombination. Moreover, the better match between the energy level of Co t_{2g} hole-acceptor states in CoFe-PBA and the VB edge of hematite modified with Pi layer will facilitate the hole transfer from the VB of hematite to the CoFe-PBA OEC. The synergy between the Pi layer and CoFe−PBA on hematite is thus crucial to suppress the recombination of the surface accumulated holes with the conduction band electrons and to accelerate the water oxidation kinetics (Scheme 1c).

4. Conclusion

Hematite photoanodes were fabricated and modified with phosphate ions (Pi) interfacial layer and CoFe−Prussian blue analogue (CoFe−PBA) oxygen evolution catalyst (OEC). They have been studied by using XRD, SEM, XPS, TPC, EIS, and IMPS techniques. The Mott−-Schottky plots analysis revealed that the Pi layer induces the formation of oxygen vacancies (i.e., in agreement with the XPS results) and reduces the space charge layer width. The Mott−Schottky analysis together with the bandgap calculation indicated that the entire band structure of hematite is anodically shifted upon modification with the Pi layer. Moreover, the DFT simulations suggested that the Pi layer drifts the electrostatic potential of the hematite surface toward more negative potential and thus attracts and accumulates the photogenerated holes at the surface. This is crucial to energetically promote the transfer of the photogenerated holes from the valance band of hematite to the Co t_{2g} hole-acceptor states in CoFe−PBA, where they can be efficiently involved in the water oxidation process. It is worth mentioning that the modification of hematite with only Pi layer or CoFe−PBA OEC showed lower PEC activity evincing the vibrant role of the Pi interfacial layer. The TPC measurements revealed that the synergy between the Pi layer and CoFe−PBA prolongs the lifetime of the photogenerated holes. The IMPS results confirmed that via the interfacial layer approach, the rate constant of surface recombination could be greatly suppressed, whereas the efficiency of charge transfer could be greatly enhanced. The charge separation and charge transfer tests performed in the presence of electron donors (Na_2SO_3) suggested that the CoFe−PBA OEC has a dual function (i.e., passivation and catalysis).

CRediT authorship contribution statement

Abdul Zeeshan Khan: Methodology, Formal analysis, Writing – original draft. **Tarek A Kandiel:** Conceptualization, Methodology, Writing – review & editing,Supervision. **Safwat Abdel-Azeim:** DFT

simulations. **Tahir Naveed Jahangir:** Methodology, Writing – original draft. **Khalid Alhooshani:** Supervision.

Declaration of Competing Interest

The authors declare that they have no known competing financial interests or personal relationships that could have appeared to influence the work reported in this paper.

Acknowledgments

The authors acknowledge the support provided by the Deanship of Scientific Research (DSR) at King Fahd University of Petroleum & Minerals (KFUPM) through Project No. DF201010. S. A. thanks the Supercomputer Shaheen at King Abdullah University of Science & Technology (KAUST) in Thuwal, Saudi Arabia, for using its computational resources.

Appendix A. Supporting information

Supplementary data associated with this article can be found in the online version at doi:10.1016/j.apcatb.2021.121014.

References

[1] M.G. Walter, E.L. Warren, J.R. McKone, S.W. Boettcher, Q. Mi, E.A. Santori, N. S. Lewis, Solar water splitting cells, Chem. Rev. 110 (2010) 6446–6473.
[2] H.-M. Li, Z.-Y. Wang, H.-J. Jing, S.-S. Yi, S.-X. Zhang, X.-Z. Yue, Z.-T. Zhang, H.-X. Lu, D.-L. Chen, Synergetic integration of passivation layer and oxygen vacancy on hematite nanoarrays for boosted photoelectrochemical water oxidation, Appl. Catal. B: Environ. 284 (2021), 119760.
[3] F. Le Formal, E. Pastor, S.D. Tilley, C.A. Mesa, S.R. Pendlebury, M. Grätzel, J. R. Durrant, Rate law analysis of water oxidation on a hematite surface, J. Am. Chem. Soc. 137 (2015) 6629–6637.
[4] C. Das, P. Roy, M. Yang, H. Jha, P. Schmuki, Nb doped TiO_2 nanotubes for enhanced photoelectrochemical water-splitting, Nanoscale 3 (2011) 3094–3096.
[5] A.Y. Ahmed, M.G. Ahmed, T.A. Kandiel, Hematite photoanodes with size-controlled nanoparticles for enhanced photoelectrochemical water oxidation, Appl. Catal. B: Environ. 236 (2018) 117–124.
[6] D.-D. Qin, C.-L. Tao, S.A. Friesen, T.-H. Wang, O.K. Varghese, N.-Z. Bao, Z.-Y. Yang, T.E. Mallouk, C.A. Grimes, Dense layers of vertically oriented WO_3 crystals as anodes for photoelectrochemical water oxidation, Chem. Commun. 48 (2012) 729–731.
[7] J.H. Kim, J.S. Lee, Elaborately modified $BiVO_4$ photoanodes for solar water splitting, Adv. Mater. 31 (2019), 1806938.
[8] C. Li, Z. Luo, T. Wang, J. Gong, Surface, bulk, and interface: rational design of hematite architecture toward efficient photo-electrochemical water splitting, Adv. Mater. 30 (2018), 1707502.
[9] K. Sivula, F. Le Formal, M. Grätzel, Solar water splitting: progress using hematite α-Fe_2O_3 photoelectrodes, ChemSusChem 4 (2011) 432–449.
[10] H.-J. Ahn, M.-J. Kwak, J.-S. Lee, K.-Y. Yoon, J.-H. Jang, Nanoporous hematite structures to overcome short diffusion lengths in water splitting, J. Mater. Chem. A 2 (2014) 19999–20003.
[11] M. Barroso, S.R. Pendlebury, A.J. Cowan, J.R. Durrant, Charge carrier trapping, recombination and transfer in hematite (α-Fe_2O_3) water splitting photoanodes, Chem. Sci. 4 (2013) 2724–2734.
[12] Y. Zhang, S. Jiang, W. Song, P. Zhou, H. Ji, W. Ma, W. Hao, C. Chen, J. Zhao, Nonmetal p-doped hematite photoanode with enhanced electron mobility and high water oxidation activity, Energy Environ. Sci. 8 (2015) 1231–1236.
[13] D. Cao, W. Luo, J. Feng, Y. Zhao, Z. Li, z zou, Cathodic shift of onset potential for water oxidation on a Ti^{4+} doped Fe_2O_3 photoanode by suppressing back reaction, Energy Environ. Sci. 7 (2013) 752–759.
[14] M. Li, Y. Yang, Y. Ling, W. Qiu, F. Wang, T. Liu, Y. Song, X. Liu, P. Fang, Y. Tong, Y. Li, Morphology and doping engineering of sn-doped hematite nanowire photoanodes, Nano Lett. 17 (2017) 2490–2495.
[15] S. Shen, P. Guo, D.A. Wheeler, J. Jiang, S.A. Lindley, C.X. Kronawitter, J.Z. Zhang, L. Guo, S.S. Mao, Physical and photoelectrochemical properties of Zr-doped hematite nanorod arrays, Nanoscale 5 (2013) 9867–9874.
[16] S.D. Tilley, M. Cornuz, K. Sivula, M. Grätzel, Light-induced water splitting with hematite: Improved nanostructure and iridium oxide catalysis, Ange. Chem. Inter. Ed. 49 (2010) 6405–6408.
[17] P. Dias, L. Andrade, A. Mendes, Hematite-based photoelectrode for solar water splitting with very high photovoltage, Nano Energy 38 (2017) 218–231.
[18] D.K. Zhong, M. Cornuz, K. Sivula, M. Grätzel, D.R. Gamelin, Photo-assisted electrodeposition of cobalt-phosphate (Co-Pi) catalyst on hematite photoanodes for solar water oxidation, Energy Environ. Sci. 4 (2011) 1759–1764.
[19] D.K. Zhong, D.R. Gamelin, Photoelectrochemical water oxidation by cobalt catalyst ("Co-Pi")/α-Fe_2O_3 composite photoanodes: Oxygen evolution and resolution of a kinetic bottleneck, J. Am. Chem. Soc. 132 (2010) 4202–4207.
[20] Y.B. Park, J.H. Kim, Y.J. Jang, J.H. Lee, M.H. Lee, B.J. Lee, D.H. Youn, J.S. Lee, Exfoliated nife layered double hydroxide cocatalyst for enhanced photoelectrochemical water oxidation with hematite photoanode, ChemCatChem 11 (2019) 443–448.
[21] J.Y. Kim, J.-W. Jang, D.H. Youn, G. Magesh, J.S. Lee, A stable and efficient hematite photoanode in a neutral electrolyte for solar water splitting: Towards stability engineering, Adv. Energy Mater. 4 (2014), 1400476.
[22] P.-Y. Tang, L.-J. Han, F.S. Hegner, P. Paciok, M. Biset-Peiró, H.-C. Du, X.-K. Wei, L. Jin, H.-B. Xie, Q. Shi, T. Andreu, M. Lira-Cantú, M. Heggen, R.E. Dunin-Borkowski, N. López, J.R. Galán-Mascarós, J.R. Morante, J. Arbiol, Boosting photoelectrochemical water oxidation of hematite in acidic electrolytes by surface state modification, Adv. Energy Mater. 9 (2019), 1901836.
[23] M. Wang, H. Wang, Q. Wu, C. Zhang, S. Xue, Morphology regulation and surface modification of hematite nanorods by aging in phosphate solutions for efficient pec water splitting, Int. J. Hydrog. Energy 41 (2016) 6211–6219.
[24] B. Moss, F.S. Hegner, S. Corby, S. Selim, L. Francàs, N. López, S. Giménez, J.-R. Galán-Mascarós, J.R. Durrant, Unraveling charge transfer in cofe prussian blue modified $BiVO_4$ photoanodes, ACS Energy Lett. 4 (2019) 337–342.
[25] L. Han, P. Tang, Á. Reyes-Carmona, B. Rodríguez-García, M. Torréns, J.R. Morante, J. Arbiol, J.R. Galan-Mascaros, Enhanced activity and acid ph stability of prussian blue-type oxygen evolution electrocatalysts processed by chemical etching, J. Am. Chem. Soc. 138 (2016) 16037–16045.
[26] F.S. Hegner, I. Herraiz-Cardona, D. Cardenas-Morcoso, N. López, J.-R. Galán-Mascarós, S. Gimenez, Cobalt hexacyanoferrate on $BiVO_4$ photoanodes for robust water splitting, ACS Appl. Mater. Interfaces 9 (2017) 37671–37681.
[27] F.S. Hegner, D. Cardenas-Morcoso, S. Giménez, N. López, J.R. Galan-Mascaros, Level alignment as descriptor for semiconductor/catalyst systems in water splitting: The case of hematite/cobalt hexacyanoferrate photoanodes, ChemSusChem 10 (2017) 4552–4560.
[28] A.Z. Khan, T.A. Kandiel, S. Abdel-Azeim, K. Alhooshani, Boosting the efficiency of water oxidation via surface states on hematite photoanodes by incorporating Bi^{3+} ions, Sustain. Energy Fuels 4 (2020) 4207–4218.
[29] T.A. Kandiel, Mechanistic investigation of water oxidation on hematite photoanodes using intensity-modulated photocurrent spectroscopy, J. Photochem. Photobiol. A: Chem. 403 (2020), 112825.
[30] Z. Chen, T. Deutsch, H. Dinh, K. Domen, K. Emery, A. Forman, N. Gaillard, R. Garland, C. Heske, T. Jaramillo, A. Kleiman-Shwarsctein, E. Miller, K. Takanabe, J. Turner, Photoelectrochemical water splitting: Standards, experimental methods, and protocols, Photoelectrochemical water splitting, Springer,, New York, 2013, pp. 7–16.
[31] S. Trasatti, O.A. Petrii, Real surface area measurements in electrochemistry, J. Electroanal. Chem. 327 (1992) 353–376.
[32] K. Shimizu, J.-F. Boily, Electrochemical properties and relaxation times of the hematite/water interface, Langmuir 30 (2014) 9591–9598.
[33] G. Kresse, J. Hafner, Ab initio molecular-dynamics simulation of the liquid-metal-amorphous-semiconductor transition in germanium, Phys. Rev. B 49 (1994) 14251–14269.
[34] A. Kay, I. Cesar, M. Graetzel, New benchmark for water photooxidation by nanostructured alpha-fe2o3 films, J. Am. Chem. Soc. 128 (2006) 15714–15721.
[35] D. Bersani, P.P. Lottici, A. Montenero, Micro-raman investigation of iron oxide films and powders produced by sol–gel syntheses, J. Raman Spectrosc. 30 (1999) 355–360.
[36] A. Sunny, A. Thirumurugan, K. Balasubramanian, Laser induced fano scattering, electron–phonon coupling, bond length and phonon lifetime changes in α-Fe_2O_3 nanostructures, Phys. Chem. Chem. Phys. 22 (2020) 2001–2009.
[37] H.-L. Lee, N. Flynn, X-ray photoelectron spectroscopy, in: D.R. Vij (Ed.), Handbook of applied solid state spectroscopy, Springer, US, 2006, pp. 485–507.
[38] Y. Feng, X. Wang, P. Dong, J. Li, L. Feng, J. Huang, L. Cao, L. Feng, K. Kajiyoshi, C. Wang, Boosting the activity of prussian-blue analogue as efficient electrocatalyst for water and urea oxidation, Sci. Rep. 9 (2019) 15965.
[39] J.-C. Dupin, D. Gonbeau, P. Vinatier, A. Levasseur, Systematic xps studies of metal oxides, hydroxides and peroxides, Phys. Chem. Chem. Phys. 2 (2000) 1319–1324.
[40] Z. Wang, X. Mao, P. Chen, M. Xiao, S.A. Monny, S. Wang, M. Konarova, A. Du, L. Wang, Understanding the roles of oxygen vacancies in hematite-based photoelectrochemical processes, Angew. Chem. Int. Ed. 58 (2019) 1030–1034.
[41] Z. Wang, F. Fan, S. Wang, C. Ding, Y. Zhao, C. Li, Bridging surface states and current-potential response over hematite-based photoelectrochemical water oxidation, RSC Adv. 6 (2016) 85582.
[42] A.Y. Ahmed, M.G. Ahmed, T.A. Kandiel, Modification of hematite photoanode with cobalt based oxygen evolution catalyst via bifunctional linker approach for efficient water splitting, J. Phys. Chem. C. 120 (2016) 23415–23420.
[43] E.J. Elzinga, D.L. Sparks, Phosphate adsorption onto hematite: An in situ atr-ftir investigation of the effects of ph and loading level on the mode of phosphate surface complexation, J. Coll. Interface Sci. 308 (2007) 53–70.
[44] L.M. Peter, Energetics and kinetics of light-driven oxygen evolution at semiconductor electrodes: The example of hematite, J. Solid State Electrochem. 17 (2013) 315–326.
[45] D. Wang, Y. Zhang, C. Peng, J. Wang, Q. Huang, S. Su, L. Wang, W. Huang, C. Fan, Crystallinity engineering of hematite nanorods for high-efficiency photoelectrochemical water splitting, Adv. Sci. 2 (2015), 1500005.
[46] L. Zhang, E. Reisner, J.J. Baumberg, Al-doped ZnO inverse opal networks as efficient electron collectors in $BiVO_4$ photoanodes for solar water oxidation, Energy Environ. Sci. 7 (2014) 1402–1408.

[47] X. Yang, R. Liu, C. Du, P. Dai, Z. Zheng, D. Wang, Improving hematite-based photoelectrochemical water splitting with ultrathin tio2 by atomic layer deposition, ACS Appl. Mater. Interfaces 6 (2014) 12005–12011.
[48] C. Baumanis, D.W. Bahnemann, TiO_2 thin film electrodes: Correlation between photocatalytic activity and electrochemical properties, J. Phys. Chem. C. 112 (2008) 19097–19101.
[49] Z. Zhang, H. Nagashima, T. Tachikawa, Ultra-narrow depletion layers in a hematite mesocrystal-based photoanode for boosting multihole water oxidation, Angew. Chem. Inter. Ed. 59 (2020) 9047–9054.
[50] C. Li, A. Li, Z. Luo, J. Zhang, X. Chang, Z. Huang, T. Wang, J. Gong, Surviving high-temperature calcination: ZrO_2-induced hematite nanotubes for photoelectrochemical water oxidation, Angew. Chem. Inter. Ed. 56 (2017) 4150–4155.
[51] T.A. Kandiel, M.G. Ahmed, A.Y. Ahmed, Physical insights into band bending in pristine and Co-Pi-modified $BiVO_4$ photoanodes with dramatically enhanced solar water splitting efficiency, J. Phys. Chem. Lett. 11 (2020) 5015–5020.
[52] E.A. Ponomarev, L.M. Peter, A generalized theory of intensity modulated photocurrent spectroscopy (imps), J. Electroanal. Chem. 396 (1995) 219–226.
[53] D. Cardenas-Morcoso, A. Bou, S. Ravishankar, M. García-Tecedor, S. Gimenez, J. Bisquert, Intensity-modulated photocurrent spectroscopy for solar energy conversion devices: What does a negative value mean? ACS Energy Lett. 5 (2020) 187–191.
[54] L.H. Wong, M.G. Ahmed, M. Zhang, Y.F. Tay, S.Y. Chiam, Surface modification of hematite photoanodes with ceox co-catalyst for improved photoelectrochemical water oxidation kinetics, Chemsuschem 13 (2020) 5489–5496.